Composites Part B 229 (2022) 109467

Contents lists available at ScienceDirect

Composites Part B

journal homepage: www.elsevier.com/locate/compositesb

Highly aligned aramid nanofibrillar nanocomposites for enhanced dynamic mechanical properties

Donggeun Lee [a], Jinhan Cho [b,c], Jeong Gon Son [c,d], Bongjun Yeom [a,*]

[a] Department of Chemical Engineering, Hanyang University, Seoul, 04763, Republic of Korea
[b] Department of Chemical and Biological Engineering, Korea University, Seoul, 02841, Republic of Korea
[c] KU-KIST Graduate School of Converging Science and Technology, Korea University, Seoul, 02841, Republic of Korea
[d] Soft Hybrid Materials Research Center, Korea Institute of Science and Technology (KIST), Seoul, 02792, Republic of Korea

ARTICLE INFO

Keywords:
Aramid nanofiber
Dynamic mechanical properties
Stiffness
Damping
Alignment
Anisotropy
Interfacial interaction

ABSTRACT

Nanocomposites with aligned nanofillers have received significant attention because of their excellent mechanical properties. However, because of the difficulty in identifying interfacial interactions in mechanical responses, the anisotropic dynamic mechanical properties of aligned nanocomposites, especially those with high reinforcement contents, are not fully understood. In this study, aligned aramid nanofiber/poly(vinyl alcohol) (ANF/PVA) nanocomposites with a nanofiller volume fraction of 48% are fabricated by using the swelling-assisted stretching method. This method enabled high degree of alignment of the ANF nanofibers with a sheath of PVA matrix. Enhancement of mechanical strength and stiffness is attributed to improvements of interfacial interactions between aligned ANFs and PVA via effective stress transfer. The damping properties are varied by activation of different dissipation modes, such as the stick–slip and reversible matrix-tearing at the interfaces, that are dependent to the loading angle relative to the nanofiber alignment direction. Resultant viscoelastic properties evaluated by the weight-adjusted viscoelastic figure of merits, the combination of stiffness and damping properties, exceed the conventional limit line up to three folds in magnitude. Deepening the understanding of anisotropic dynamic mechanical responses is required for designing aligned nanocomposite materials for mechanical and electronic applications.

1. Introduction

The structures of biomaterials, such as the bones and muscles of vertebrates, the exoskeletons of arthropods and mollusks, and the cells comprising woods have recently drawn significant attentions owing to their ultrahigh mechanical properties [1–4]. Most of them have highly ordered internal structure with high reinforcement contents, 50–90% in volume, that are attributed to origin of the exceptional mechanical responses by effective stress transfer [5,6]. Aligned nanocomposites are promising for applications that require high strength and light weight, such as artificial muscles [7], protection gear for sports and militaries [8], and constituent elements for buildings [9] and mobile platforms [10]. Additionally, the aligned functional nanofillers with high reinforcement contents can be served as charge [11] and thermal [12] pathways, that are beneficial to the enhancement of electrical, ionic and thermal conductivities along with mechanical properties. These could be applied in electronic devices [13], biomedical [14], protective [15], thermal conduction [16] and energy storage applications [17–19]. Inspired by these internal structures, nanocomposites with aligned reinforcing nanofillers such as carbon nanotubes [20,21], cellulose nanofibers [22], and aramid nanofibers (ANFs) [23–25] were fabricated by stretching or electrospinning processes to induce alignment of the reinforced fillers in polymeric matrices [26]. However, manufacture of the aligned nanocomposites with high volume fractions are still limited and the relationship between the mechanical properties and anisotropically aligned structures, especially that associated with the dynamic mechanical behaviors of such materials, is not yet fully understood.

Recently, damping property, mechanical energy dissipation, of the nanocomposites has received growing attentions to protect vibration sensitive component in the various types of electronic, photonic, and acoustic systems from external stress, impact, and vibrational fatigues [27–30]. Damping properties are known to have an intrinsic trade-off relationship with stiffness, as illustrated in the Ashby plot [31,32]. For instance, most metals and ceramics have high stiffness and low damping,

* Corresponding author.
E-mail address: byeom@hanyang.ac.kr (B. Yeom).

https://doi.org/10.1016/j.compositesb.2021.109467
Received 7 September 2021; Received in revised form 5 November 2021; Accepted 6 November 2021
Available online 11 November 2021

while the opposite holds for viscoelastic rubbery polymers. The viscoelastic figure of merit (VFOM), which is expressed by the product of stiffness and damping, $E^*\cdot\tan\delta$, cannot exceed 0.6 GPa for most conventional materials [33–35]. It is also effective to consider density for the practical use of the VFOM, expressed by the product of stiffness and damping properties per unit density, with an upper limit of $(E^*/\rho)\cdot(\tan\delta)^{0.5} = 0.8$ for most of engineering materials [30]. A few exceptional cases of composite materials have been reported that exceed this weight-adjusted VFOM limit [30,34–36]. The incorporation of vanadium dioxide particles in a tin matrix yields an exceptionally high $(E^*/\rho)\cdot(\tan\delta)^{0.5}$ of 1.19 owing to the excellent stiffness of the reinforcing particles [35]. In addition, artificial nanocomposites that mimic the internal nanostructures of the enamel layer of teeth have shown excellent combinations of stiffness and damping properties, achieving a $(E^*/\rho)\cdot(\tan\delta)^{0.5}$ up to 2.51 [30]. A multi-walled carbon nanotube-modified epoxy demonstrated high stiffness and damping behavior with $(E^*/\rho)\cdot(\tan\delta)^{0.5}$ reaching 3.62 [36]. The interfacial interactions among constituent elements have been indicated as important factors that determine the dynamic mechanical responses of nanocomposites. Mechanisms such as the zipper model [37], stick–slip [38–40], and matrix tearing [41] have been used to describe interfacial damping mechanisms. However, the role of interfacial interactions, especially in the anisotropic dynamic mechanical responses of aligned nanocomposites with high reinforcement contents, are not yet fully understood because of the difficulty in discerning interfacial phenomena in mechanical responses.

ANF nanocomposites have received considerable attention owing to their excellent mechanical properties and excellent chemical and thermal stabilities. They have robust one-dimensional fibrillary nanostructures with strong interchain interactions provided by hydrogen bonding between amide groups, and their dimensions are typically 5–200 nm in diameter with an aspect ratio of ~500 [42]. ANFs have been used as reinforcements with various polymer matrices including polyurethane [43], poly(vinyl alcohol) (PVA) [44,45], polyacrylic acid [46], and epoxy [47,48]. Composites have been fabricated by various methods such as layer-by-layer (LBL) assembly [43], solvent exchange [44], vacuum-assisted filtration [46], and spin coating [47]. Such reinforced nanocomposites exhibit outstanding mechanical and energy dissipation properties owing to the interchain interactions between the reinforcements and the matrix. For instance, ANF/PVA nanofilms fabricated by solution casting exhibit tensile strength up to 140 MPa, stiffness up to 6 GPa, and tanδ of 0.12, with a weight-adjusted VFOM value of 1.59 [45]. Nanocomposites made by the LBL deposition of ANFs and epoxy resin exhibit ultimate strengths of up to 505 MPa, stiffness of 15 GPa, tanδ of 0.11, and weight-adjusted VFOM value of 3.32 [47]. Their potential application areas are diverse, including high-end thermal insulation [49], electrical insulation [50], battery separators [51] and flexible electronics [52]. However, nanocomposites with aligned ANFs have rarely been reported because of the difficulty arising from the rigidity of ANFs. Only few approaches have realized aligned ANF nanocomposites by electrospinning [23,24] and stretching [25]. However, the electrospinning of ANFs requires high temperatures and voltages, and electrospun ANFs possess poor mechanical properties with stress and stiffness up to 70 MPa and 1.1 GPa [23], respectively, owing to the large fiber size distribution and low degree of alignment, which possibly suppress the enhancement of mechanical properties. In addition, ANF and PVA were utilized to fabricate aligned nanocomposites with high portion of nanoclay ~50 wt% for high strength and foldable stability nanocomposites with superior optical properties [25]. To the best of our knowledge, studies on the anisotropic dynamic mechanical properties of ANF nanocomposites, especially when ANF contents are high, have not yet been reported.

Herein, we report the effects of interfacial interactions on the mechanical and dynamic mechanical properties of aligned ANF/PVA nanocomposites with high nanofiller content. We performed field-emission scanning electron microscopy (FE-SEM), wide and small angle X-ray scatterings (WAXS and SAXS) to study the effect of stretching to alignments of nanofiber and polymeric matrices, and Fourier-transform infrared spectroscopy (FT-IR), broadband dielectric spectroscopy (BDS) and dynamic mechanical analysis (DMA) to interpret interfacial interactions to understand their contributions to the dynamic mechanical responses. The direct mixing of aramid nanoseed dispersions with PVA solutions enhanced the intermolecular integration, resulting ANF/PVA nanocomposites with high volumetric contents of ANFs (up to 48%). Highly aligned ANF nanocomposites were prepared by swelling-assisted stretching of the nanocomposites without the use of heat or applied voltage, resulting in the highly dispersed ANF/PVA nanofibrillar structures without presence of the coagulation of nanofillers. The alignment of ANFs caused a drastic increase in the mechanical properties of mechanical strength and stiffness owing to the effective stress transfer through the ANF/PVA nanofibers. We also found that the damping responses of the anisotropic nanocomposites were significantly affected by the designated loading angle (φ) of 0°, 45°, and 90° relative to the nanofiber alignment direction, that could be attributed to activation of different damping mechanisms of the stick–slip and the reversible matrix tearing. The weight-adjusted VFOM values measured to be 2.21 at 1 Hz and 2.43 at 30 Hz. These values considerably outperform over upper limit value (0.8) about three folds in magnitude, and comparable to the highest values from recent reports in a range of 2.5–3.6 [30,36,37]. To the best of our knowledge, the work described in this paper is the first systematic investigation of the anisotropic dynamic mechanical properties of ANF nanocomposites. It would serve as a novel example in the interpretation of dynamic mechanics for aligned nanocomposites, and helps to identify the nature of dynamic mechanical properties in aligned fiber-reinforced nanocomposites with high reinforcement contents and enables their versatile use in several applications.

2. Experimental section

2.1. Materials

The Kevlar fibers (aramid fibers) used in this work were purchased from the Thread Exchange. Poly(vinyl alcohol) (PVA, M_w ~145,000) and potassium hydroxide (KOH) were purchased from Sigma-Aldrich. Dimethyl sulfoxide (DMSO) was obtained from Daejung Chemicals.

2.2. Preparation of aramid nanoseed dispersion

The aramid nanoseed solution was prepared using the procedure described in a previous study [53]. To obtain a 1 wt% aramid nanoseed solution, 1 g of bulk Kevlar fiber and 1 g of KOH were added to DMSO, which was magnetically stirred for 2 weeks at 27 °C until a dark red solution was obtained.

2.3. Fabrication of ANF/PVA nanocomposite films

ANF/PVA nanocomposites were prepared by a solution-casting method (Fig. 1a). First, 1 g of PVA was dissolved in deionized (DI) water by heating to 100 °C for 1 h to obtain a 1 wt% PVA aqueous solution. Different concentrations of PVA solutions were added to a 0.02 wt% diluted aramid nanoseed dispersion with a volume ratio of 9:10 to obtain ANF/PVA mixed suspensions. These mixtures were cast onto Teflon plates and dried at 70 °C to prepare the ANF/PVA nanocomposites. ANF volume fractions of 35 vol% and 48 vol% were obtained for the ANF/PVA nanocomposites with PVA solution concentrations of 0.1 wt% and 0.05 wt%, respectively. The ANF/PVA nanocomposite films were washed with DI water and dried under vacuum at 50 °C for 24 h.

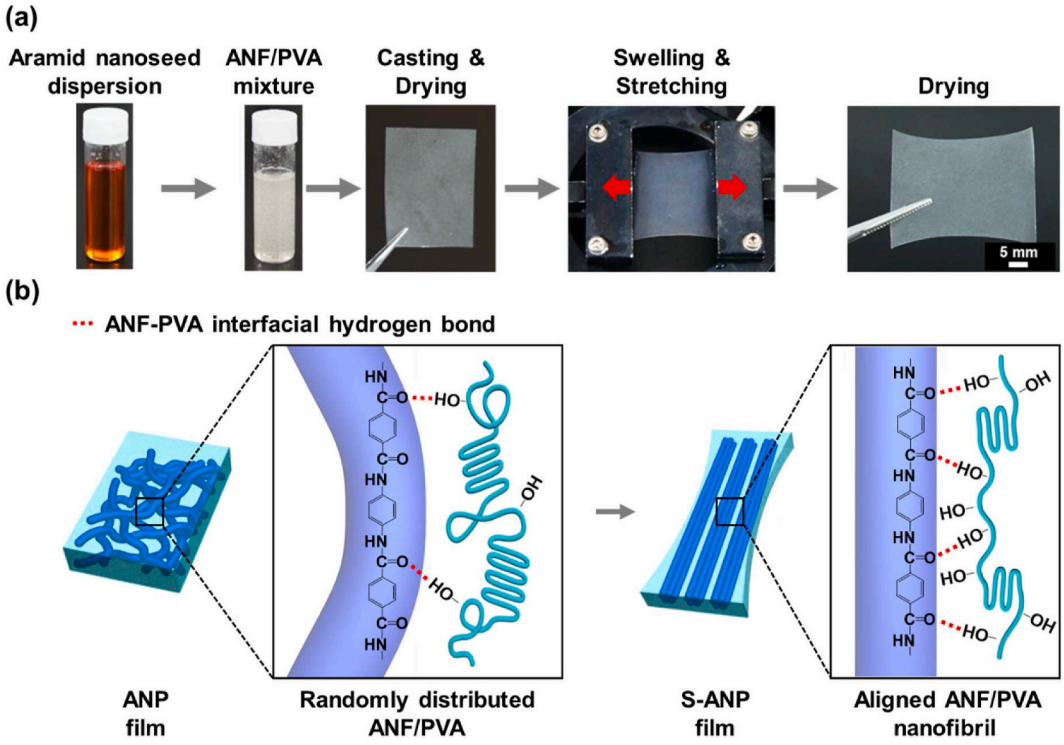

Fig. 1. Schematics of (a) sample preparation of the ANF/PVA nanocomposites and (b) the change in the interfacial interaction upon stretching.

2.4. Fabrication of aligned ANF/PVA nanocomposite films by stretching

Aligned ANF/PVA nanocomposites were obtained by a swelling-assisted stretching method (Fig. 1a). A custom-made uniaxial strain stage was used to stretch the ANF/PVA nanocomposites. After mounting the ANF/PVA nanocomposites, the nanocomposites were swelled for 30 min with DI water. The swollen nanocomposites were stretched to obtain highly aligned ANF/PVA nanocomposites with the applied strains of 50% and 35% for swollen ANP35 and ANP48, respectively. After drying at room temperature for 30 min, the samples were further dried under vacuum at 50 °C for 24 h. For the mechanical tests, the stretched nanocomposites were cut at angles of 0°, 45°, and 90° relative to the fiber alignment direction.

2.5. Characterization

Thermogravimetric analysis (TGA) was conducted using a TA Instruments SDT Q600 under a nitrogen atmosphere with a heating rate of 10 °C/min from 25 °C to 500 °C. Raman spectra were obtained using a Horiba Scientific LabRAM HR Evolution Raman spectrometer with 785 nm excitation. Cross-sectional images of the ANF nanocomposites were obtained using FE-SEM (Hitachi S-4800). Atomic force microscopy (AFM) images were obtained using Parksystems XE100 and transmission electron microscopy (TEM) images were obtained using JEOL JEM-2100 F to reveal the nanoscale morphology. The aramid nanoseed dispersion was further diluted 10–60 fold and drop casted on Si wafer, followed by drying at 70 °C to obtain clear ANF images for AFM and TEM. SAXS images and azimuthal scan intensities were acquired using a Xenocs Xeuss 2.0 to identify the alignment of ANFs. WAXS was conducted using Bruker D8 Discover to confirm the alignment of PVA crystals at the molecular level. FT-IR spectra were recorded using a Thermo Nicolet iS50 to identify changes in the characteristic peaks of the functional moieties. Tensile tests, dynamic frequency sweeps and temperature sweeps were conducted using TA Instruments DMA 850 to investigate the mechanical, dynamic mechanical properties. The ultimate strength of each film was recorded as the highest stress value in the stress–strain curves. These were coincident with the strength at failure for most cases, except for the PVA samples, which showed maximum strengths at yield points. Potassium chloride (KCl) saturated solution was used to maintain relative humidity up to 84%. Saturated KCl solution was sealed in a container with PVA and ANP samples and stored for an additional 3 days after reaching 84% relative humidity [54]. BDS was performed by a Scribner Associates Inc. BDS 20 apparatus at 25 °C, with the applied AC voltage of 1 V over the range of 10 μHz to 10^6 Hz to investigate the relaxation behaviors. Samples were cut into circular shape with a diameter of 3 cm, and tested between two copper plates. Additional silver coating was performed to increase the contact at the sample surface. The moisture contents of measured samples were 3% for ANP nanocomposites and 4% for pristine ANF and PVA film (Fig. S2).

3. Results and discussion

3.1. Fabrication and characterization of ANF/PVA nanocomposites

We employed the simple direct mixing of diluted aramid nanoseed solutions in DMSO and PVA aqueous solutions to fabricate ANF/PVA nanocomposites (Fig. 1a) instead of using infiltration methods to avoid coagulation near the surface [55]. Preparation began with dissolving aramids in dimethyl sulfoxide with potassium hydroxide. Homogeneous aramid nanoseed dispersions were formed because of the electrostatic repulsion among the deprotonated aramid nanoseeds [56]. A distinct color change of the solution was observed with the incorporation of the PVA solution, indicating that the water molecules in the PVA solution facilitated the reprotonation of the aramid nanoseeds, resulting in formation of ANFs in mixtures. ANF/PVA nanocomposites were obtained by casting and drying ANF/PVA suspensions. Successful reprotonation was confirmed by the absence of notable differences in the characteristic Raman scattering peaks of amide groups in the aramids at 1578 cm^{-1} and 1660 cm^{-1} in comparing the peaks of pristine aramid fiber and ANF/PVA nanocomposites (Fig. S1). TGA results was used to calculate the content of ANFs in the nanocomposites (Fig. S2). The volume fractions of ANF in the nanocomposites were estimated using the following

formula [57]:

$$v_{ANF} = \frac{w_{ANF}\rho_{ANF}}{\rho_{ANF}(1 - w_{ANF}) + w_{ANF}\rho_{PVA}} \quad (1)$$

where v_{ANF} is the volume fraction of ANFs, w_{ANF} is the weight fraction of ANFs obtained from TGA, and ρ_{ANF} and ρ_{PVA} are the densities of ANFs and PVA, respectively. ANF volume fractions of 35% and 48% were observed in the ANF/PVA nanocomposites with different PVA solution concentrations; these samples were denoted as ANP35 and ANP48, respectively. With increase of PVA concentration, the mixture appeared hazier suspensions indicating greater degree of coagulation of ANF and PVA in the mixture. (Fig. S3). It is noted that homogeneous films obtained for the PVA concentrations of 0.05 and 0.1% were further utilized in this study, that are corresponding to the ANF volume fractions of 48% and 35%, respectively. ANF nanocomposite films with volume fractions of <35% and >48% were excluded because of the uneven distribution of ANF in the PVA matrix due to high degree of coaguation and brittleness of the fabricated films, respectively (Fig. S4).

Highly aligned ANF/PVA nanocomposites were prepared by swelling-assisted stretching. The dried ANF/PVA nanocomposites could be swelled and softened by exposure to water majorly due to swelling of PVA matrix incorporated with ANF nanofibers. This enabled stretching of the ANP films up to ultimate strain of 70 and 50% for ANP35 and ANP48 films, respectively. Such elongations were impossible for pristine ANF films and other types of ANF/PVA nanocomposites prepared by infiltration method due to presence of brittle nature of ANF fillers. The swollen ANP films were stretched to strain of 50 and 35% for ANP35 and ANP48 film, respectively, followed by drying in stretched conditions, resulting in highly aligned ANP nanocomposites (Fig. 1a). The stretched samples are denoted as S-PVA, S-ANP35, and S-ANP48 with their nanofiller contents. Even with such swelling-induced stretching, integration of ANFs with PVA are highly maintained, and it is presumed that interfacial interactions between ANFs and PVA are strong enough to hold such mechanical strain induced alignment under swelled state (Fig. 1b).

3.2. Nanostructure characterization of ANF/PVA nanocomposites

The nanoscale morphology of the pristine ANF was revealed by AFM and TEM. Pristine ANF exhibited nanofibrillar morphologies in network structures with diameter of 3.2 ± 0.3 nm and 7.1 ± 1.7 nm for AFM and TEM, respectively (Fig. S5). To better understand the nanoscale morphology of the ANF/PVA nanocomposites, FE-SEM was conducted. Fibrous network structures of ANFs with voids, which were not found in the cross-sections of PVA and S-PVA (Figs. S6a and b), were observed in the ANF film (Fig. 2a). Their average fiber diameter was ~38 nm, within the typical diameter range of ANFs [42]. The voids seen in the pristine ANF films were not visible in the cross-sectional images of the ANF/PVA nanocomposites (Fig. 2b), and their fiber diameter was increased to ~94 nm, possibly due to wrapping with the PVA matrix. When S-ANP48 was cut longitudinally with respect to the stretching direction (Fig. 2c and d), most of the nanofibrillar structures were observed to lie parallel to the stretching direction with a high degree of alignment. In contrast, when S-ANP48 was cut transversely with respect to the stretching direction (Fig. 2e and f), circular cross-sections of the nanofibers were observed, implying that the nanofibers were successfully aligned. These appearances could be also observed with low magnification images (Fig. 2c and e). After stretching, the diameter of the observed nanofibrils was ~136 nm, which was higher than those of pristine nanofibers and ANFs in randomly oriented nanocomposites. To further identify the thickening of the nanofiber diameter, S-ANP48 was partially cut transversely and pulled out to reveal interfacial morphology at the rupture surface (Fig. 2g and h). Reduction of the nanofiber diameter at fibrillary ends are clearly observed and the size of tip diameter, ~35 nm, is close to that of pristine ANF, marked with the red dotted circles (Fig. 2h). It is

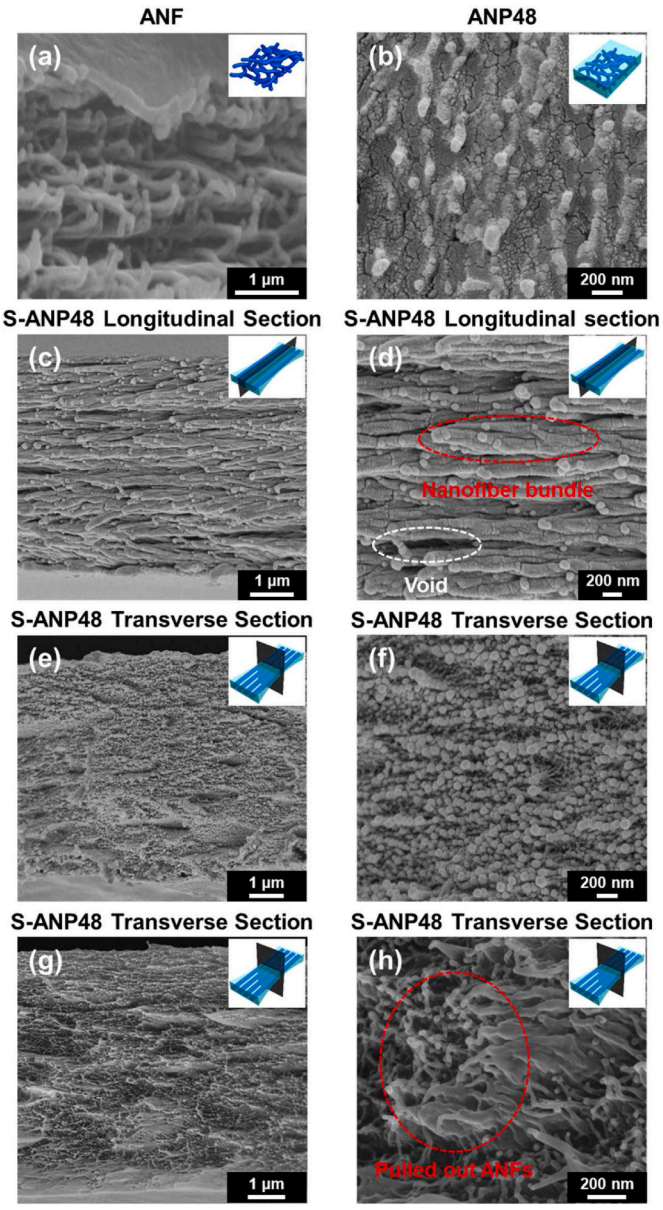

Fig. 2. FE-SEM cross-sectional images of (a) ANF, (b) ANP48, and (c–h) S-ANP48 samples. For the S-ANP48 sample, (c, d) longitudinal and (e, f) transverse cross-sections and (g, h) transverse cross-sections at ruptured region.

presumed that the observed ANFs were pulled out from the PVA matrix under applied stress. Additionally, the ANF/PVA nanofibers were expected to form in bundled shapes, as marked by the red dotted circle (Fig. 2d), under the applied stretching process. The formation of voids was observed as marked by the white dotted circle (Fig. 2d), which could be attributed to the inclusion of some misaligned nanofibers in the geometrically restricted aligned nanofiber networks.

The anisotropic features of the aligned ANF/PVA nanocomposites were confirmed by SAXS (Fig. 3). The transmittance of X-ray was measured with normal incidence to the sample surface with the stretching direction parallel to the horizontal line. The 2D SAXS patterns of the ANP48 sample exhibited isotropic scattering patterns and flat azimuthal angle profiles (Fig. 3a). On the contrary, in the case of S-ANP48, distortions of the scattering patterns and scattering peaks located at 90° and 270° in the azimuthal profiles clearly indicated that the ANF/PVA nanofibers in the stretched nanocomposites were oriented along the stretching direction, yielding anisotropic features (Fig. 3b). Meanwhile, no significant distortion of the diffraction patterns was

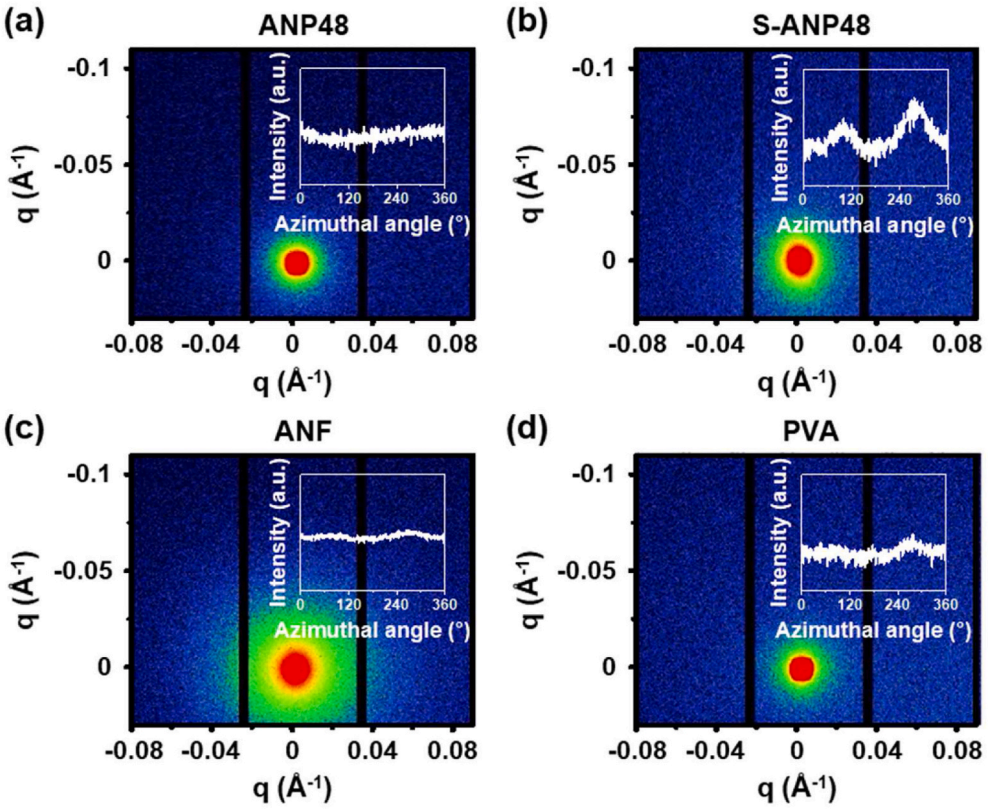

Fig. 3. 2D SAXS results of (a) ANP48, (b) S-ANP48, (c) ANF, (d) PVA. Inset plots show azimuthal intensity profiles at $q = 0.012$ Å^{-1}. Stretching direction of the samples was aligned in parallel to the horizontal axis of the detector.

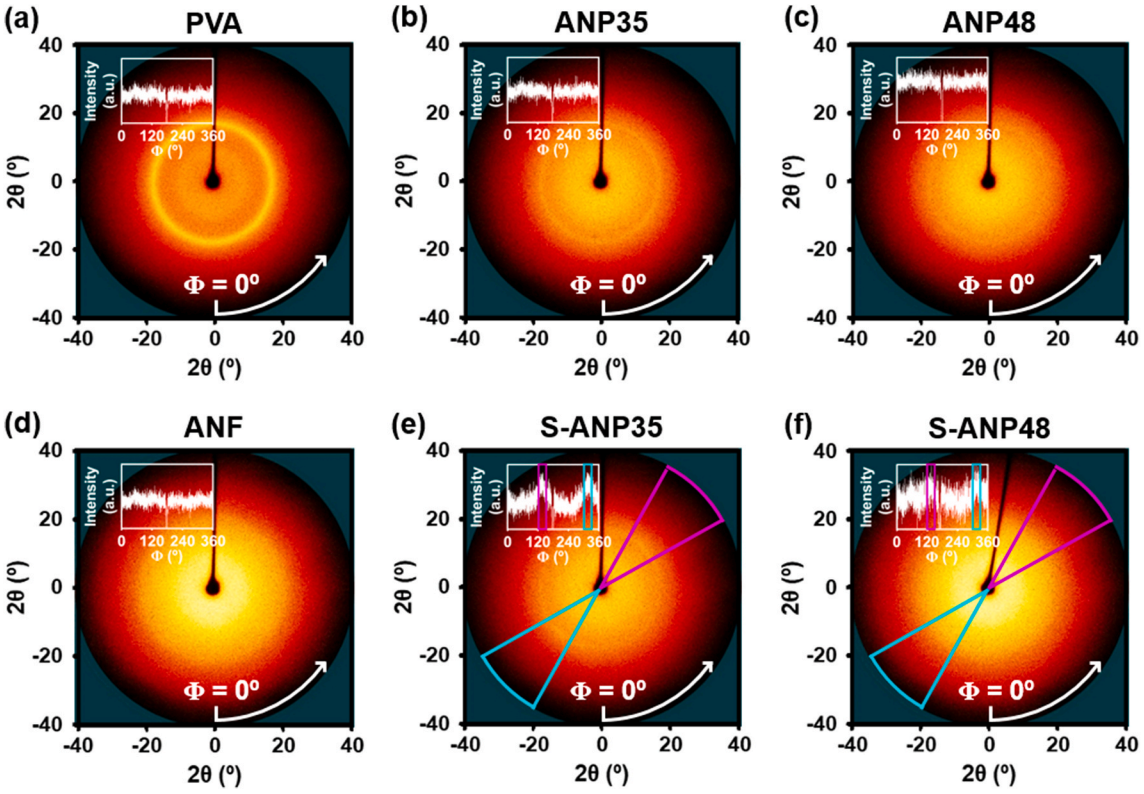

Fig. 4. 2D WAXS results of (a) PVA (b) ANP35, (c) ANP48, (d) ANF (e) S-ANP35 and (f) S-ANP48. Inset plots show azimuthal intensity profiles at $2\theta = 19.3°$. Stretching direction of the samples was aligned in parallel to the horizontal axis of the detector.

observed in the ANFs, PVA films, and non-stretched ANF/PVA nanocomposites with flat azimuthal intensity profiles, which indicated random distributions (Fig. 3c and d).

2D WAXS tests of pristine ANF, PVA and ANF/PVA nanocomposites were performed to confirm alignment of PVA crystal domains at the molecular level (Fig. 4 and Fig. S7). The 2D WAXS pattern of the pristine PVA sample exhibited isotropic ring scattering with maximum intensity at $2\theta = 19.3°$, which was assigned to the (101) plane of PVA crystal lattice (Fig. 4a). Inset shows the azimuthal angle (Φ) profile scanned at $2\theta = 19.3°$ with flatten feature. Pristine ANF exhibited broad isotropic ring scattering patterns with maximum intensity at $2\theta = 23.2°$ (Fig. 4d). ANP35 and ANP48 samples also exhibited similar isotropic ring patterns in Fig. 4b and c, that are mainly attributed to (101) plane of PVA crystals as shown in the 2theta plots in Figs. S7c–d. Azimuthal angle profiles also do not present any noticeable peaks except dips from beam stopper around $\Phi = 180°$. ANF peaks for the ANP samples present in minor portion as weak shoulders near $2\theta = 23.2°$ in Figs. S7c–d. Therefore we focused on the change of the PVA (101) peaks for analysis of all ANP and stretched samples.

On the other hands, the azimuthal angle profiles of S-ANP35 and S-ANP48 samples have two peaks around $\Phi = 130°$ and 310° for both samples (Fig. 4e and f). Peak areas in the insets are highlighed with colored boxes in purple and green colors to indicate $\Phi = 130°$ and 310° regions, respectively. Same regions are marked in Fig. 4e and f, but with full theta angles, for guidance. Although it is difficult to find distinct anisotropic arc patterns in the 2D patterns of Fig. 4e and f due to weak intensities, the scattering intensity profiles with the azimuthal angle range of 300° ~330° and 210° ~240° show differences at PVA (101) peak positions (Figs. S7g–h). S-ANP48 sample shows less anisotropic features than S-ANP35 sample probably due to less content of PVA. These results indicate that (101) planes of PVA crystals are perpendicularly oriented to the azimuthal angle of 130° and 310° directions. As PVA molecules lie in the *c*-axis direction at the lattice and the drawing directions are parallell to the azimuthal angle of 90° and 180° direction, these results indicate that PVA molecules in crystal domains are oriented to the drawing direction as depicted in Fig. S8 [58].

3.3. Evaluation of interfacial interactions of ANF/PVA nanocomposites

FT-IR results provided insights into the interfacial interactions between the ANFs and PVA. The characteristic peaks of ANF and PVA were observed in the ANF/PVA nanocomposites, indicating that homogeneous nanocomposites were formed via direct mixing (Fig. S9). The effects of the incorporation of ANFs in the PVA matrix (Fig. 5a–c) and alignment of ANF/PVA nanofibers (Fig. 5d–f) on the interfacial interactions were investigated. A distinct blue-shift of the C═O and C–N stretching bands in the amide groups of ANF was observed upon increasing the PVA content (Fig. 5a and b) [44]. We presume that these spectral changes originated from the partial replacement of interfacial hydrogen bonds between amides (ANF-ANF) and between amides and hydroxyl groups (ANF-PVA). Since blue shift generally indicates the strengthening of bond strength according to the hooke's law [59], such spectral change might be attributed to the strengthened bond strength of amide groups in the aramid chains, that caused by weakening of interchain interactions to another aramid or PVA chains [43]. In contrast, red-shift for the C–O stretching band in the hydroxyl groups of PVA was observed upon increasing the ANF content to 35 vol% in minor degree of ~2 cm^{-1} (Fig. 5c). When the ANF contents is increased to 48 vol%, it is barely changed. These spectral changes might be attributed to the replacement of weaker PVA–PVA hydrogen bonds by relatively strong ANF–PVA hydrogen bonds with increased ANF content, which would weaken the C–O vibration energy. After stretching, a red-shift of the C═O and C–N stretching bands was observed (Fig. 5d and e). We presume that alignment of ANFs and PVA nanofibrillar structures enabled increases of interfacial interactions of aramid groups in ANFs, causing reduction vibration energy of C═O and N–H bonds of ANFs [60]. The blue-shift of the C–O stretching band upon stretching (Fig. 5f) might be attributed to the decreases of intramolecular hydrogen bonds in PVA

Table 1
Crystallinity of PVA and ANF/PVA nanocomposites.

	Crystallinity by FT-IR [%]
PVA	48.2
S-PVA	42.3
ANP35	43.4
S-ANP35	41.4
ANP48	41.1
S-ANP48	37.1

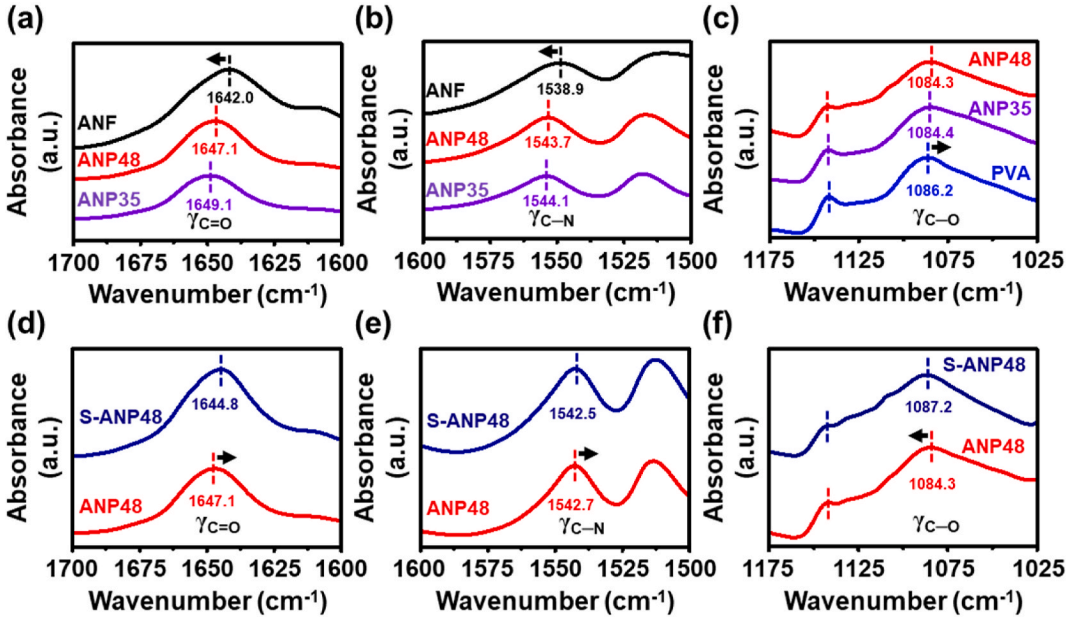

Fig. 5. FT-IR spectra. (a) C═O and (b) C–N stretching vibration modes for ANF and ANF/PVA nanocomposites. (c) C–O stretching vibration modes for PVA and ANF/PVA nanocomposites. (d) C═O, (e) C–N, and (f) C–O stretching vibration modes for ANP48 and S-ANP48 samples.

crystals [61]. ANP35 and S-ANP35 showed FT-IR spectra similar to those of ANP48 and S-ANP48 (Fig. S10).

The degree of crystallinity (χ_c) of PVA was calculated from FT-IR (Table 1), obtained by normalizing the intensity of the crystalline band at 1141 cm^{-1} to the intensity of the C–O stretching band at 1086 cm^{-1} in the FT-IR spectra (Fig. 5c and f, S10b and d) [62]. Compared with pure PVA, the PVA in the composites was decreased in crystallinity with increasing ANF content (Fig. 5c). The incorporation of ANFs into the PVA matrix interrupted the intrinsic arrangement of the PVA chains through the formation of strong ANF–PVA hydrogen bonds [63]. Such interactions hindered the formation of crystalline domains in the PVA chain, thus yielding lower crystallinity. A reduction in the crystallinity was observed upon stretching of ANP48 (Fig. 5f), indicating that the PVA crystal arrays inside the crystallites lost their intrinsic arrangement with stretching owing to the further interactions between ANFs and PVA. The profiles of ANP35 and S-ANP35 showed similar features to those of ANP48 and S-ANP48 (Fig. S10 b and d).

Dielectric analysis was conducted to further investigate the local chain motion in the ANF nanocomposite films (Fig. 6). The Havriliak–Negami (HN) function was adopted to analyze the dielectric loss spectra and to obtain quantitative information [64]. The detailed deconvolution principles for dielectric loss are described in Supporting Information with Fig. S11. A single HN function and conductivity process accurately describes the data for ANF, PVA, and S-PVA (Figs. S11a–c). However, two HN functions and a conductivity term were needed to describe the β relaxation of ANF and PVA in the dielectric spectra of the ANF/PVA nanocomposites (Figs. S11d–g). Between the two relaxations, the β relaxation of ANFs was considered slower than that of PVA (Fig. 6c and d) for the following reasons. First, relaxation of pristine ANFs is much slower than those of pristine PVA (Fig. 6c and d). In addition, both ANFs and PVA exhibited β relaxation near room temperature [65,66] and the contribution of interfacial polarization was no longer visible at high reinforcement contents [66]. For easier comparison, enlarged spectra of ANP48 and S-ANP48 are shown in Fig. 6a and b. The conductivity exponentially decreased and two peaks arising from the β relaxations of PVA and ANF were observed; the fitted results matched the experimental data. To reveal each relaxation, the fitted results of the ANF and PVA β relaxations were separately shown in Fig. 6c and d, respectively. By incorporation of ANFs in PVA matrix, the β relaxations of the ANF and PVA peaks shifted to a higher frequency. These results might be attributed to the interruption of intrinsic arrangement of PVA due to the strong ANF-PVA hydrogen bonds, as discussed in FT-IR analysis. By increasing the ANF content from 35 to 48 vol%, the β relaxations of the ANF and PVA peaks do not present significant changes in peak positions. Upon stretching, the β relaxation of the ANF and PVA shifted to a higher frequency (Fig. 6c and d). These results indicate that faster local chain motions of ANF and PVA with easier relaxations. The details of β relaxation upon stretching will be discussed in the dynamic mechanical analysis part.

3.4. Mechanical properties of ANF/PVA nanocomposites

DMA analysis as a function of temperature was conducted to compare the strength of hydrogen bonds between ANFs and PVA (Fig. 7 and Table S1). Pristine ANF exhibited γ relaxation at −24 °C, β relaxation at 52 °C, and β* relaxation at 203 °C (Fig. 7a) [65]. β* relaxation is associated with rotational modes of dissociation and re-bonding of hydrogen bondings of amide groups in crystalline state with strong intermolecular bonds for the ANF-ANF bonds, while β relaxation indicates the motions of amorphous amide groups [65]. Pristine PVA exhibited β relaxation at 57 °C and α relaxation at 104 °C (Fig. 7b) [66]. ANF/PVA nanocomposites exhibited broad relaxation peak below 0 °C, around 50 °C and above 140 °C, which can be assigned to the ANF γ relaxation, mixture of β relaxations of ANF and PVA, and mixture of ANF β* and PVA α relaxations, respectively (Fig. 7c–f). α relaxation of the pristine ANF was not taken into account due to high temperature

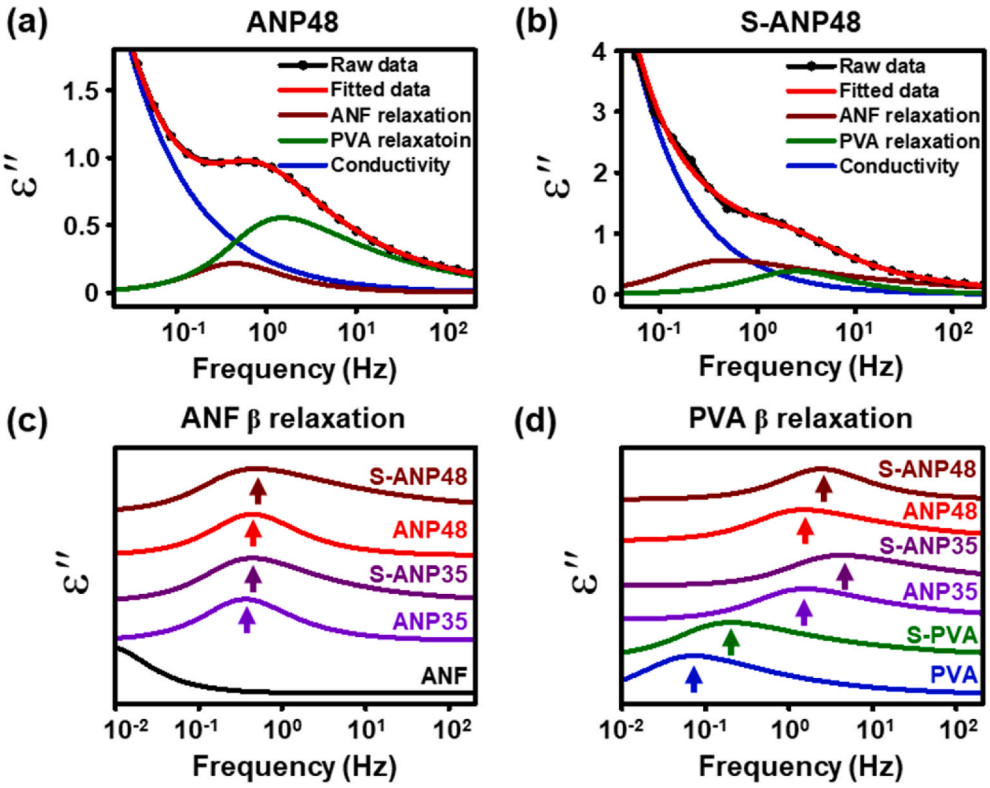

Fig. 6. Dielectric test results. Dielectric loss data of (a) ANP48 and (b) S-ANP48 are shown with fitting results with two Havriliak–Negami (HN) functions and a conductivity term. ANF, PVA and ANF/PVA nanocomposite films with β relaxations from (c) ANF and (d) PVA contributions for the samples with different ANF volume contents and for stretched samples.

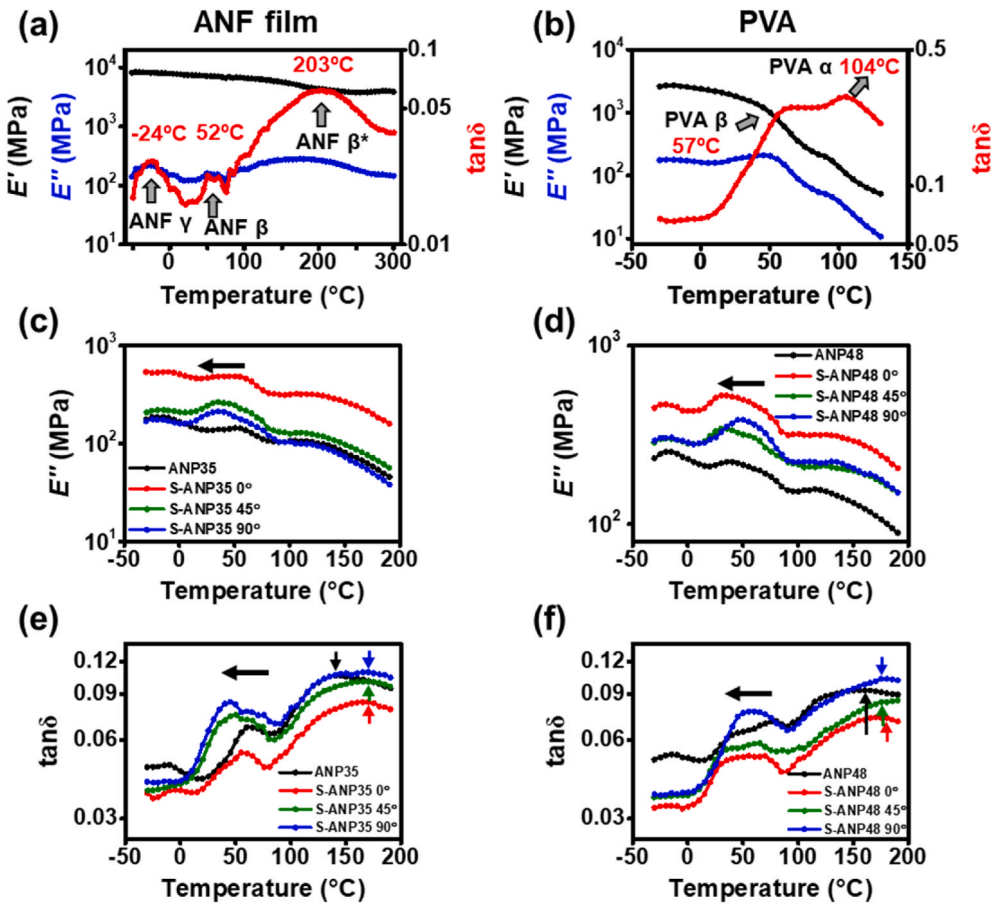

Fig. 7. Storage moduli, loss moduli and tanδ results of (a) ANF and (b) PVA as a function of temperature. (c–d) Loss moduli and (e–f) tanδ values of ANP nanocomposites and stretched samples as a function of temperature with various loading angles.

transition around 460 °C [67]. ANP35 and ANP48 samples have broad tanδ peaks at 100–200 °C regions with maximum intensities located at 143 °C and 161 °C, respectively, as shown in Fig. 7e and f. Higher α relaxation temperature of PVA with increasing ANF contents indicates that the movement of main chains was restricted due to the increased number of stronger interfacial hydrogen bonds of ANF-PVA upon increasing ANF contents. Furthermore, PVA α relaxation temperature for ANP35 and ANP48 which were much higher than the α relaxation temperature of pristine PVA of 104 °C, which might be attributed to the stronger hydrogen bonds of ANF-PVA than PVA-PVA. Considering that ANF β* relaxation temperature becomes lower at the ANP samples due to formation of ANF-PVA interactions, the relative strength of interfacial hydrogen bonds can be assigned in the order of ANF-ANF > ANF-PVA > PVA-PVA.

Furthermore, to investigate anisotropic features of aligned ANF/PVA nanocomposites, the relaxation temperatures of ANP and S-ANP samples were analyzed. S-ANP35 and S-ANP48 samples exhibited the mixed relaxations of PVA α transition and ANF β* transitions around 168 °C and 176 °C, respectively. (Fig. 7e and f, and Table S1). Although the relaxation temperatures were not changed upon increasing alignment angle due to the strong interaction, but were much higher than randomly distributed ANP samples. We presume that the alignments of ANFs and PVA enabled increases of interfacial interactions, require higher energy for relaxations than randomly distributed nanocomposites. On the another hand, when ANP samples were stretched, β transitions associated with the local chain movement were relatively shifted to lower temperatures as indicated by black lateral arrows in Fig. 7e and f. These results with easier relaxations are coincident with the dielectric results. When loading angle φ is increased for the S-ANP samples (Fig. 7e and f), the β relaxation of ANF and PVA have tendency to become shifted to relatively lower temperature, indicating more active relaxations of the local pendent groups of PVA and amide groups of ANF in amorphous region [66]. It is also noted that increase of loading angle φ for the S-ANP samples is accompanied with increase of tanδ intensities for the entire temperature range, that are coincident to anisotropic damping properties observed in the frequency sweep DMA tests, which will be discussed later.

Uniaxial tensile tests were conducted to investigate the reinforcement effect of the ANFs and to understand their anisotropic features (Fig. 8a–e and Table 2). Fig. 8 graphs show selective mechanical test results among more than 5 tests. Mechanical test results in Table 2 are tabulated with averaged values with errors. Stretched samples were prepared to examine tensile behaviors with certain designated tilted loading angles φ of 0°, 45°, and 90° relative to the nanofiber alignment direction; these were denoted as S-ANP48 0°, S-ANP48 45°, and S-ANP48 90°, respectively (Fig. S12). The effects of the incorporation of ANFs in the PVA matrix and the alignments of ANF/PVA nanofibers on the uniaxial tensile tests are shown in Fig. 8a and b, respectively. Stress–strain curves of the pristine PVA matrix are also shown in Fig. 8c. The incorporation of ANFs in PVA improved the mechanical properties. In the case of ANP48, the mechanical properties were improved to the ultimate stress σ_u of 118 ± 9 MPa and Young's modulus E of 3.4 ± 0.4 GPa (Fig. 8a). Upon stretching, in case of S-ANP48, σ_u and E of S-ANP48 0° were increased up to 296 ± 23 MPa and 11.1 ± 0.9 GPa (Fig. 8b), which were much higher than those of the ANF film (σ_u of 231 ± 29 MPa and E of 8.8 ± 1.2 GPa; Fig. 8a). The improvement of mechanical properties is majorly contributed by straightened ANFs with directional alignments and effective stress transfer between these ANFs and the PVA matrix. The improved stress transfer could be attributed to the network structures of ANFs in the nanocomposites and increase in interfacial

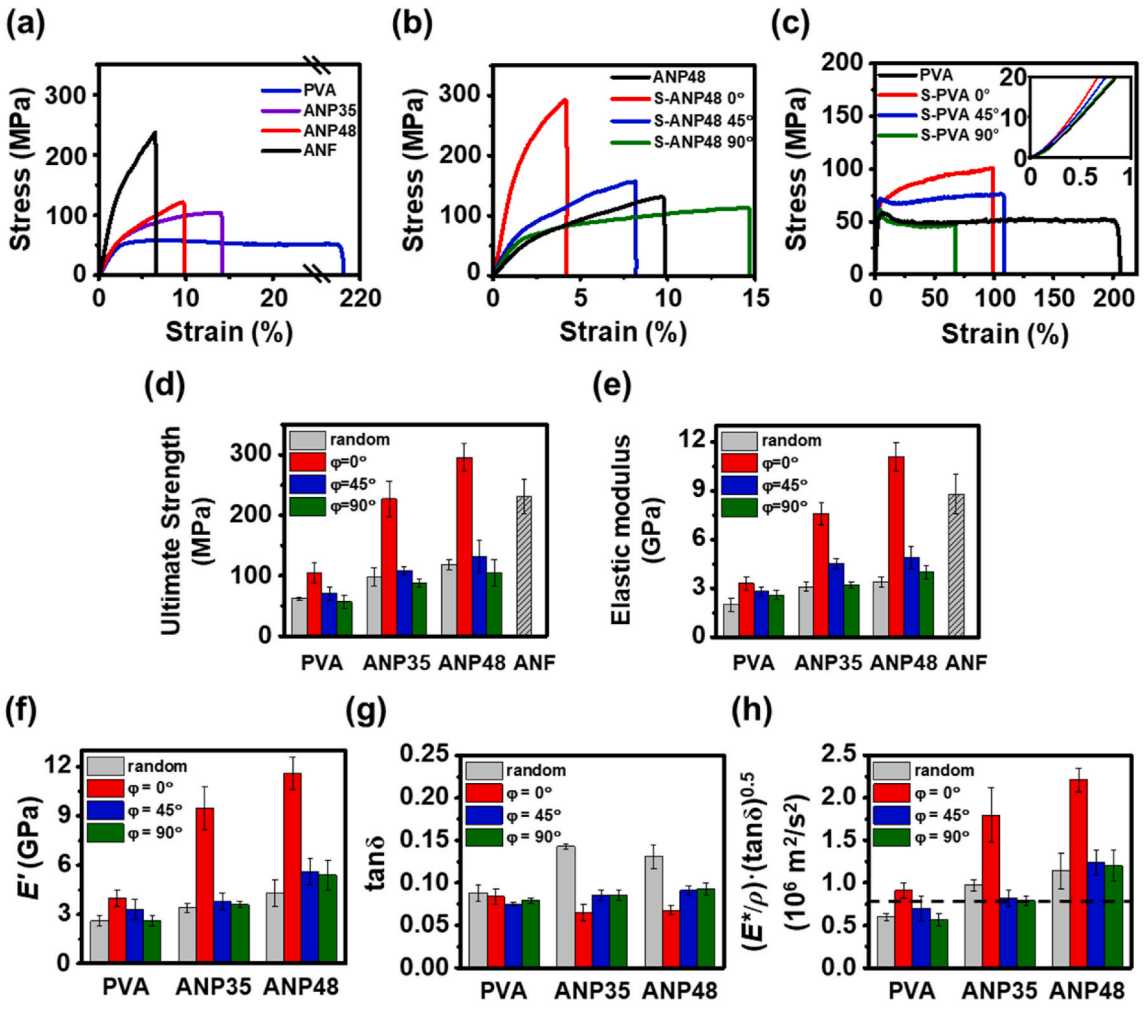

Fig. 8. Tensile test results. Stress–strain curves for (a) ANF, PVA and ANF/PVA nanocomposites with various volume contents, (b) ANP48 and S-ANP48, (c) PVA and S-PVA with various loading angles. Inset in (c) shows magnified stress–strain curve in the region of low tensile strain. Summary plots of (d) ultimate strengths and (e) elastic moduli of PVA, ANF and ANF/PVA nanocomposites at different loading angles. Dynamic mechanical analysis results of (f) storage moduli and (g) tanδ, (h) (E^*/ρ) $(\tan\delta)^{0.5}$ of PVA and ANF/PVA nanocomposites obtained at 1 Hz with various loading angles.

Table 2
Summary of the tensile test results of PVA, ANF, and ANF/PVA nanocomposites.

	Ultimate strain [%]	Ultimate strength [MPa]	Elastic modulus [GPa]	Toughness [MJ/m^3]
PVA	206 ± 7	62 ± 3	2.0 ± 0.4	121.7 ± 15.7
S-PVA 0°	100 ± 20	105 ± 17	3.3 ± 0.4	109.2 ± 49.3
S-PVA 45°	108 ± 10	71 ± 11	2.8 ± 0.3	60.6 ± 16.8
S-PVA 90°	66 ± 26	57 ± 11	2.6 ± 0.3	36.7 ± 10.9
ANP35	12 ± 3	98 ± 15	3.1 ± 0.3	10.5 ± 4.0
S-ANP35 0°	7 ± 1	227 ± 30	7.6 ± 0.7	10.0 ± 2.5
S-ANP35 45°	17 ± 3	108 ± 6	4.5 ± 0.3	12.6 ± 1.9
S-ANP35 90°	16 ± 2	88 ± 6	3.2 ± 0.2	11.5 ± 2.1
ANP48	13 ± 3	118 ± 9	3.4 ± 0.4	10.4 ± 2.3
S-ANP48 0°	5 ± 1	296 ± 23	11.1 ± 0.9	10.0 ± 2.6
S-ANP48 45°	8 ± 1	132 ± 26	4.9 ± 0.7	7.4 ± 1.0
S-ANP48 90°	16 ± 5	105 ± 22	4.0 ± 0.4	10.1 ± 4.2
ANF	7 ± 1	231 ± 29	8.8 ± 1.2	10.4 ± 2.1

interactions of ANFs with PVA, as described earlier. By increasing the loading angle φ of S-ANP48 from 0° to 90°, σ_u and E decreased to 105 ± 22 MPa and 4.0 ± 0.4 GPa, respectively. The decrease in E upon increasing the loading angle φ in ANF/PVA nanocomposites could be attributed to the tearing of the PVA matrix near the voids, which can impede effective stress transfer. Meanwhile, E of perpendicularly oriented nanocomposites is slightly higher than randomly distributed one. These results might be attributed to the stronger interfacial interactions between nanofillers and matrix after alignment [68]. These observations were consistent with the mechanical test results for ANP35 and S-ANP35 (Fig. S13). A similar tendency was observed for S-PVA (Fig. 8c), but less pronounced variation was observed compared to the S-ANP48 case. S-PVA showed a 1.7-fold increase for both σ_u and E, while S-ANP48 samples showed a 2.5-fold increase in σ_u and 3.3-fold increase in E. With changes in the loading angle to 90°, S-PVA shows a 1.8-fold decrease in σ_u and 1.3-fold decrease in E, compared to the S-ANP48 case with a 2.8-fold decrease for both σ_u and E. This variation can be attributed to the reinforcement effects of the straightened ANFs and the ANF/PVA nanofibers.

DMA tests as a function of frequency were conducted to examine the anisotropic damping behavior of the ANF/PVA nanocomposites (Fig. 8f–h and Table 3). The storage modulus (E') (Fig. 8f), which reflects the material's capability to store energy elastically, showed a tendency similar to that of E from the uniaxial tensile test results (Fig. 8e). The

Table 3
Summary of the dynamic mechanical analysis data of PVA and ANF/PVA nanocomposites at 1 Hz.

	Storage modulus [GPa]	tanδ	$(E^*/\rho)\cdot(\tan\delta)^{0.5}$ [10^6 m^2/s^2]
PVA	2.6 ± 0.3	0.088 ± 0.010	0.60 ± 0.04
S-PVA 0°	4.0 ± 0.5	0.084 ± 0.009	0.91 ± 0.09
S-PVA 45°	3.3 ± 0.6	0.075 ± 0.002	0.70 ± 0.14
S-PVA 90°	2.6 ± 0.3	0.079 ± 0.003	0.57 ± 0.07
ANP35	3.4 ± 0.3	0.143 ± 0.003	0.97 ± 0.07
S-ANP35 0°	9.5 ± 1.3	0.065 ± 0.010	1.80 ± 0.32
S-ANP35 45°	3.8 ± 0.5	0.085 ± 0.006	0.82 ± 0.10
S-ANP35 90°	3.6 ± 0.2	0.085 ± 0.006	0.79 ± 0.05
ANP48	4.3 ± 0.8	0.131 ± 0.014	1.14 ± 0.21
S-ANP48 0°	11.6 ± 1.0	0.068 ± 0.005	2.21 ± 0.14
S-ANP48 45°	5.6 ± 0.8	0.091 ± 0.005	1.24 ± 0.15
S-ANP48 90°	5.4 ± 0.9	0.093 ± 0.007	1.20 ± 0.18

damping ratio or tanδ, which is the ratio between the loss modulus and storage modulus and which reflects the relative degree of energy dissipation or damping by a viscoelastic material, exhibited different tendencies from those observed in the tensile test results (Fig. 8g). DMA tests of pristine ANF samples prepared by the casting method were difficult to conduct owing to the brittleness of the samples under dynamic deformation. Spin-coated pristine ANFs were reported to exhibit a stiffness of 11 GPa and tanδ of 0.06 [47]. Incorporation of ANFs in PVA significantly increased the tanδ value relative to that of PVA. For instance, ANP48 exhibited a tanδ value of 0.131 ± 0.014. It is presumed that the reversible detachment and attachment of randomly orientated ANFs at the interfaces of ANF/PVA can cause much greater energy dissipation than that occurring in the pristine PVA matrix [37]. Stretched nanocomposites exhibited decreased tanδ values. For instance, the tanδ of S-ANP48 0° decreased to 0.068 ± 0.005. We attribute this to the fact that the energy dissipation caused by the reversible stick and slippage of aligned ANF/PVA nanofibers [38–40] (as illustrated in Fig. S14a) is weaker than that caused by the interfacial detachment and attachment in randomly oriented ANF samples [37]. However, tanδ of S-ANP48 90°, 0.093 ± 0.007, was greater than that of S-ANP48 0°. Increasing the loading angle φ from 0° to 90° reduces interfacial shear effects [40], but can allow enhanced energy dissipation through the reversible tearing of the PVA matrix near the voids existing between the nanofibers (Fig. S14b) [41]. Increases in β relaxations for ANF and PVA are also responsible for increase of damping properties with increase of loading angle as observed in Fig. 7c–f. In the case of the PVA and S-PVA samples, the variation in damping properties was not as pronounced as that of the ANF/PVA nanocomposites. Additionally, at a higher frequency of 30 Hz, the tendencies of variations in stiffness and tanδ were coincident with those observed at 1 Hz (Figs. S15–17).

The moisture contents of the ANP samples were around 3% that determined by weight loss around 100 °C from TGA measurement (Fig. S3). Water contents were controlled by using the humidity control chambers (See details in Experimental section). Both of ANP35 and S-ANP35 samples with higher water content of 7% presented lower storage modulus and higher tanδ values than the samples with lower water content of 3% (Figs. S18–S19 and Table S3).

The viscoelastic properties of materials are characterized by the weight-adjusted VFOM, expressed by the product of stiffness and damping properties per density, $(E^*/\rho)\cdot(\tan\delta)^{0.5} = 0.8$. (Fig. 9 and Table 3). For comparison, DMA data of the samples obtained at 1 Hz are represented in Fig. 9, and data points of other materials are selectively shown with DMA measurements at a various range of frequencies. An obvious improvement in stiffness and damping was observed by the incorporation of ANFs. In the case of ANP48, the weight-adjusted VFOM increased up to 1.14 ± 0.21 at 1 Hz, from the blue to red stars in the figure. By stretching, the VFOM values were increased significantly. For instance, S-ANP48 0° had a much higher weight-adjusted VFOM value of 2.21 ± 0.14 compared to that of ANP48, from the red star to the red

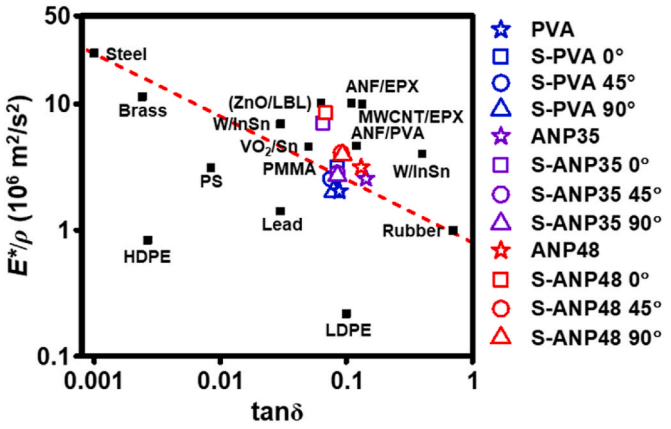

Fig. 9. Summary plot of dynamic mechanical properties obtained at 1 Hz for PVA and ANF/PVA nanocomposite samples with various volume fractions and loading angles. Limit line is shown with red dotted line of $(E^*/\rho)\cdot(\tan\delta)^{0.5} = 0.8$. Data points are plotted based on ref. 35 for VO_2/Sn at 100 Hz, ref. 30 for (ZnO/LBL) at 0.1 Hz, ref. 36 for MWCNT/EPX at 1 Hz, ref. 45 for ANF/PVA at 1 Hz, ref. 47 for ANF/EPX at 0.1 Hz and ref. 35 for other conventional materials. The weight–adjusted VFOM of the data without mentioning their density were calculated using their contents fraction and typical density. (For interpretation of the references to color in this figure legend, the reader is referred to the Web version of this article.)

square in Fig. 9. This value exceeds the merit line of conventional viscoelastic materials owing to the exceptionally high stiffness and low material density of the film. Furthermore, by increasing the frequency up to 30 Hz (Figs. S16c and S17), the weight-adjusted VFOM of S-ANP48 0° exceeded this limit by a much greater degree, reaching 2.43 ± 0.20, owing to the further improvement of E^* with increasing amplitude.

4. Conclusion

We systematically studied the anisotropic mechanical and dynamic mechanical responses of aligned ANF/PVA nanocomposites. Highly aligned ANF/PVA nanocomposites were successfully fabricated by swelling-assisted stretching. The changes in the interfacial interactions between the functional moieties of ANFs and PVA were analyzed by FT-IR analysis, dielectric analysis and dynamic mechanical analysis. The incorporation of ANFs into the PVA matrix resulted in the improvement of mechanical strength and stiffness, which might be attributed to their strong interfacial interactions. Stretching yielded aligned ANF/PVA nanofibrillar structures, with a drastic increase in mechanical strength and stiffness of the composites. On the contrary, the damping properties degraded upon stretching because the energy dissipations arising from the reversible stick–slip of the aligned ANF/PVA nanofibrils were lower than those from the interfacial detachment and attachment of randomly oriented ANFs in the ANP nanocomposites. With an increase in the loading angle φ, the energy dissipation increased owing to changes in the major energy dissipation mode from stick–slip to the reversible tearing of the PVA matrix. Increases in β relaxations for ANF and PVA also contribute to increase of damping properties at room temperature. The exceptionally high stiffness and low material density of the aligned ANP nanocomposites with loading angle $\varphi = 0$ yielded weight-adjusted VFOM values of 2.2–2.4, which are significantly higher than those of most conventional materials (<0.8). These results can be utilized for the preparation and characterization of highly aligned nanocomposites with exceptionally high stress [5,6], charge [11] and thermal [12] transport properties, which can be further employed in various electronic [13], biomedical [14], protective [15], and energy storage [17–19] applications.

CRediT author statement

Donggeun Lee: Validation, Methodology, Writing - Original draft preparation, Visualization Jinhan Cho: Conceptualization, Writing - Review & Editing Jeong Gon Son: Data Curation, Writing - Review & Editing Bongjun Yeom: Conceptualization, Supervision, Writing - Review & Editing.

Declaration of competing interest

The authors declare that they have no known competing financial interests or personal relationships that could have appeared to influence the work reported in this paper.

Acknowledgements

We gratefully acknowledge financial support from the Korea Institute of Science and Technology (KIST) Institutional Program (Project No. 2V08210). This work was supported by the National Research Foundation of Korea (NRF) grants funded by the Korean government (Ministry of Science and ICT) (nos. NRF-2021R1A2C4002523, and NRF-2019R1A4A1027627).

Appendix A. Supplementary data

Supplementary data to this article can be found online at https://doi.org/10.1016/j.compositesb.2021.109467.

References

[1] Meyers MA, McKittrick J, Chen P-Y. Structural biological materials: critical mechanics-materials connections. Science 2013;339:773–9.
[2] Wegst UGK, Bai H, Saiz E, Tomsia AP, Ritchie RO. Bioinspired structural materials. Nat Mater 2015;14:23–36.
[3] Lossada F, Hoenders D, Guo J, Jiao D, Walther A. Self-assembled bioinspired nanocomposites. Acc Chem Res 2020;53:2622–35.
[4] Huang P, Wu F, Shen B, Zheng H, Ren Q, Luo H, et al. Biomimetic porous polypropylene foams with special wettability properties. Compos B Eng 2020;190:107927.
[5] Pan X-F, Gao H-L, Lu Y, Wu C-Y, Wu Y-D, Wang X-Y, et al. Transforming ground mica into high-performance biomimetic polymeric mica film. Nat Commun 2018 91 2018;9:1–8.
[6] Mohammadi P, Aranko AS, Landowski CP, Ikkala O, Jaudzems K, Wagermaier W, et al. Biomimetic composites with enhanced toughening using silk-inspired triblock proteins and aligned nanocellulose reinforcements. Sci Adv 2019;5:eaaw2541.
[7] Choi S, Choi Y, Kim J. Anisotropic hybrid hydrogels with superior mechanical properties reminiscent of tendons or ligaments. Adv Funct Mater 2019;29:1–9.
[8] Benzait Z, Trabzon L. A review of recent research on materials used in polymer–matrix composites for body armor application. J Compos Mater 2018;52:3241–63.
[9] Li T, Song J, Zhao X, Yang Z, Pastel G, Xu S, et al. Anisotropic, lightweight, strong, and super thermally insulating nanowood with naturally aligned nanocellulose. Sci Adv 2018;4:eaar3724.
[10] Rai P, Oh S, Shyamkumar P, Ramasamy M, Harbaugh RE, Varadan VK. Nano- bio-textile sensors with mobile wireless platform for wearable health monitoring of neurological and cardiovascular disorders. J Electrochem Soc 2014;161:B3116–50.
[11] Zhao C, Niu J, Zhang Y, Li C, Hu P. Coaxially aligned MWCNTs improve performance of electrospun P(VDF-TrFE)-based fibrous membrane applied in wearable piezoelectric nanogenerator. Compos B Eng 2019;178:107447.
[12] Wang H, Ding D, Liu Q, Chen Y, Zhang Q. Highly anisotropic thermally conductive polyimide composites via the alignment of boron nitride platelets. Compos B Eng 2019;158:311–8.
[13] Huang S, Li L, Yang Z, Zhang L, Saiyin H, Chen T, et al. A new and general fabrication of an aligned carbon nanotube/polymer film for electrode applications. Adv Mater 2011;23:4707–10.
[14] Thampi S, Muthuvijayan V, Parameswaran R. Mechanical characterization of high-performance graphene oxide incorporated aligned fibroporous poly(carbonate urethane) membrane for potential biomedical applications. J Appl Polym Sci 2015;132:41809.
[15] Huang N-J, Cao C-F, Li Y, Zhao L, Zhang G-D, Gao J-F, et al. Silane grafted graphene oxide papers for improved flame resistance and fast fire alarm response. Compos B Eng 2019;168:413–20.
[16] Li M, Ali Z, Wei X, Li L, Song G, Hou X, et al. Stress induced carbon fiber orientation for enhanced thermal conductivity of epoxy composites. Compos B Eng 2021;208:108599.
[17] Cheng X-B, Huang J-Q, Zhang Q, Peng H-J, Zhao M-Q, Wei F. Aligned carbon nanotube/sulfur composite cathodes with high sulfur content for lithium–sulfur batteries. Nanomater Energy 2014;4:65–72.
[18] Chen C, Fan Y, Gu J, Wu L, Passerini S, Mai L. One-dimensional nanomaterials for energy storage. J Phys D Appl Phys 2018;51:113002.
[19] Feng M, Chi Q, Feng Y, Zhang Y, Zhang T, Zhang C, et al. High energy storage density and efficiency in aligned nanofiber filled nanocomposites with multilayer structure. Compos B Eng 2020;198:108206.
[20] Aly K, Bradford PD. Real-time impact damage sensing and localization in composites through embedded aligned carbon nanotube sheets. Compos B Eng 2019;162:522–31.
[21] Xiong L, Shuai J, Liu K, Hou Z, Zhu L, Li W. Enhanced mechanical and electrical properties of super-aligned carbon nanotubes reinforced copper by severe plastic deformation. Compos B Eng 2019;160:315–20.
[22] Wang S, Li T, Chen C, Kong W, Zhu S, Dai J, et al. Transparent, anisotropic biofilm with aligned bacterial cellulose nanofibers. Adv Funct Mater 2018;28:1707491.
[23] Chung J, Kwak S-Y. Solvent-assisted heat treatment for enhanced chemical stability and mechanical strength of meta-aramid nanofibers. Eur Polym J 2018;107:46–53.
[24] Trexler MM, Hoffman C, Smith DA, Montalbano TJ, Yeager MP, Trigg D, et al. Synthesis and mechanical properties of para-aramid nanofibers. J Polym Sci, Part B: Polym Phys 2019;57:563–73.
[25] Li H, Teng C, Zhao J, Wang J. A scalable hydrogel processing route to high-strength, foldable clay-based artificial nacre. Compos Sci Technol 2021;201:108543.
[26] Harito C, Bavykin DV, Yuliarto B, Dipojono HK, Walsh FC. Polymer nanocomposites having a high filler content: synthesis, structures, properties, and applications. Nanoscale 2019;11:4653–82.
[27] Vakilifard M, Mahmoodi MJ. Dynamic moduli and creep damping analysis of short carbon fiber reinforced polymer hybrid nanocomposite containing silica nanoparticle-on the nanoparticle size and volume fraction dependent aggregation. Compos B Eng 2019;167:277–301.
[28] Mahmoodi MJ, Vakilifard M. CNT-volume-fraction-dependent aggregation and waviness considerations in viscoelasticity-induced damping characterization of percolated-CNT reinforced nanocomposites. Compos B Eng 2019;172:416–35.
[29] Jiang Z, Wang F, Yin J, Gong S, Dai Z, Pang Y, et al. Vibration damping mechanism of CuAlMn/polymer/carbon nanomaterials multi-scale composites. Compos B Eng 2020;199:108266.
[30] Yeom B, Sain T, Lacevic N, Bukharina D, Cha S-H, Waas AM, et al. Abiotic tooth enamel. Nature 2017;543:95–8.
[31] Brodt M, Lakes RS. Composite materials which exhibit high stiffness and high viscoelastic damping. J Compos Mater 1995;29:1823–33.
[32] Ashby MF. Material selection in mechanical design. Elsevier; 2011. p. 57–96.
[33] Haldar S, Sain T, Ghosh S. A novel high symmetry interlocking micro-architecture design for polymer composites with improved mechanical properties. Int J Solid Struct 2017;124:161–75.
[34] Meaud J, Sain T, Yeom B, Park SJ, Shoultz AB, Hulbert G, et al. Simultaneously high stiffness and damping in nanoengineered microtruss composites. ACS Nano 2014;8:3468–75.
[35] Wang YC, Ludwigson M, Lakes RS. Deformation of extreme viscoelastic metals and composites. Mater Sci Eng, A 2004;370:41–9.
[36] Li M, Wang Z, Liu Q, Wang S, Gu Y, Li Y, et al. Carbon nanotube film/epoxy composites with high strength and toughness. Polym Compos 2017;38:588–96.
[37] Xu M, Futaba DN, Yamada T, Yumura M, Hata K. Carbon nanotubes with temperature-invariant viscoelasticity from -196 to 1000 C. Science 2010;330:1364–8.
[38] Keten S, Xu Z, Ihle B, Buehler MJ. Nanoconfinement controls stiffness, strength and mechanical toughness of β-sheet crystals in silk. Nat Mater 2010;9:359–67.
[39] Gardea F, Glaz B, Riddick J, Lagoudas DC, Naraghi M. Energy dissipation due to interfacial slip in nanocomposites reinforced with aligned carbon nanotubes. ACS Appl Mater Interfaces 2015;7:9725–35.
[40] Ashraf T, Ranaiefar M, Khatri S, Kavosi J, Gardea F, Glaz B, et al. Carbon nanotubes within polymer matrix can synergistically enhance mechanical energy dissipation. Nanotechnology 2018;29:115704.
[41] Gardea F, Glaz B, Riddick J, Lagoudas DC, Naraghi M. Identification of energy dissipation mechanisms in CNT-reinforced nanocomposites. Nanotechnology 2016;27:105707.
[42] Yang B, Wang L, Zhang M, Luo J, Lu Z, Ding X. Fabrication, applications, and prospects of aramid nanofiber. Adv Funct Mater 2020;30:2000186.
[43] Kuang Q, Zhang D, Yu JC, Chang Y-W, Yue M, Hou Y, et al. Toward record-high stiffness in polyurethane nanocomposites using aramid nanofibers. J Phys Chem C 2015;119:27467–77.
[44] Zhu J, Yang M, Emre A, Bahng JH, Xu L, Yeom J, et al. Branched aramid nanofibers. Angew Chem Int Ed 2017;56:11744–8.
[45] Guan Y, Li W, Zhang Y, Shi Z, Tan J, Wang F, et al. Aramid nanofibers and poly (vinyl alcohol) nanocomposites for ideal combination of strength and toughness via hydrogen bonding interactions. Compos Sci Technol 2017;144:193–201.
[46] Yang M, Cao K, Yeom B, Thouless M, Waas A, Arruda EM, et al. Aramid nanofiber-reinforced transparent nanocomposites. J Compos Mater 2015;49:1873–9.
[47] Zhu J, Watts D, Kotov NA. Gelation-assisted layer-by-layer deposition of high performance nanocomposites. Z Phys Chem 2018;232:1383–98.
[48] Nasser J, Zhang L, Sodano H. Aramid nanofiber interlayer for improved interlaminar properties of carbon fiber/epoxy composites. Compos B Eng 2020;197:108130.
[49] Yang B, Zhang M, Lu Z, Luo J, Song S, Tan J, et al. Toward improved performances of para-aramid (PPTA) paper-based nanomaterials via aramid nanofibers(ANFs) and ANFs-film. Compos B Eng 2018;154:166–74.

[50] Rahman MM, Puthirath AB, Adumbumkulath A, Tsafack T, Robatjazi H, Barnes M, et al. Fiber reinforced layered dielectric nanocomposite. Adv Funct Mater 2019;29:1900056.
[51] Tung S on, Fisher SL, Kotov NA, Thompson LT. Nanoporous aramid nanofibre separators for nonaqueous redox flow batteries. Nat Commun 2018;9:4193.
[52] Liu Y, Zhang K, Mo Y, Zhu L, Yu B, Chen F, et al. Hydrated aramid nanofiber network enhanced flexible expanded graphite films towards high EMI shielding and thermal properties. Compos Sci Technol 2018;168:28–37.
[53] Lyu J, Wang X, Liu L, Kim Y, Tanyi EK, Chi H, et al. High strength conductive composites with plasmonic nanoparticles aligned on aramid nanofibers. Adv Funct Mater 2016;26:8435–45.
[54] Young JF. Humidity control in the laboratory using salt solutions-a review. J Appl Chem 2007;17:241–5.
[55] Xu L, Zhao X, Xu C, Kotov NA. Water-rich biomimetic composites with abiotic self-organizing nanofiber network. Adv Mater 2018;30:1703343.
[56] Yang M, Cao K, Sui L, Qi Y, Zhu J, Waas A, et al. Dispersions of aramid nanofibers: a new nanoscale building block. ACS Nano 2011;5:6945–54.
[57] Kaushik AK, Podsiadlo P, Qin M, Shaw CM, Waas AM, Kotov NA, et al. The role of nanoparticle layer separation in the finite deformation response of layered polyurethane-clay nanocomposites. Macromolecules 2009;42:6588–95.
[58] Liu L-Z, Paradkar R, Bensason S. Crystal structure transformations and orientation in crosslinked elastic fibers of an ethylene-octene copolymer in response to deformation and heat treatment. J Appl Polym Sci 2013;130:3565–73.
[59] Hishikawa Yukako, Inoue Shun-ichi, Magosh Jun, Kondo Tetsuo. Novel tool for characterization of noncrystalline regions in cellulose:A FTIR deuteration monitoring and generalized two -dimensionalcorrelation spectroscopy. Biomacromolecules 2005;6:2468–73.
[60] Li Z, Zhu Y-L, Niu W, Yang X, Jiang Z, Lu Z-Y, et al. Healable and recyclable elastomers with record-high mechanical robustness, unprecedented crack tolerance, and superhigh elastic restorability. Adv Mater 2021;33:2101498.
[61] Cui S, Li L, Wang Q. Enhancing glass transition temperature and mechanical properties of poly (propylene carbonate) by intermacromolecular complexation with poly (vinyl alcohol). Compos Sci Technol 2016;127:177–84.
[62] Niu W, Zhu Y, Wang R, Lu Z, Liu X, Sun J. Remalleable, healable, and highly sustainable supramolecular polymeric materials combining superhigh strength and ultrahigh toughness. ACS Appl Mater Interfaces 2020;12:30805–14.
[63] Huan S, Bai L, Cheng W, Han G. Manufacture of electrospun all-aqueous poly(vinyl alcohol)/cellulose nanocrystal composite nanofibrous mats with enhanced properties through controlling fibers arrangement and microstructure. Polymer 2016;92:25–35.
[64] Havriliak S, Negami S. A complex plane representation of dielectric and mechanical relaxation processes in some polymers. Polymer 1967;8:161–210.
[65] Koga K, Ueta S, Takayanagi M. The structure and physical properties of aramid film prepared by electrodeposition of poly(p-phenylene terephthalamide) polyanion. Polym J 1988;20:639–47.
[66] Ghorbel N, Kallel A, Boufi S. Molecular dynamics of poly(vinyl alcohol)/cellulose nanofibrils nanocomposites highlighted by dielectric relaxation spectroscopy. Compos Part A Appl Sci Manuf 2019;124:105465.
[67] Kunugi T, Watanabe H, Hashimoto M. Dynamic mechanical properties of poly(*p*-phenyleneterephthalamide) fiber. J Appl Polym Sci 1979;24:1039–51.
[68] Dhar P, Kumar A, Katiyar V. Magnetic cellulose nanocrystal based anisotropic polylactic acid nanocomposite films: influence on electrical, magnetic, thermal, and mechanical properties. ACS Appl Mater Interfaces 2016;8:18393–409.